Chin. Phys. Lett. **39**, 018701 (2022)

Temperature-Dependent Far-Infrared Absorption in Cyclotrimethylene Trinitramine Single Crystals Using Broadband Time-Domain Terahertz Spectroscopy

Yupeng Liu(刘羽鹏)[1], Jinchun Shi(史进春)[2], and Chongyang Chen(陈重阳)[1*]

[1]*Institute of Modern Physics, Fudan University, Shanghai 200433, China*
[2]*The Peac Institute of Multiscale Sciences, Chengdu 610031, China*

(Received 22 September 2021; accepted 17 December 2021; published online 29 December 2021)

We investigate the absorption properties of cyclotrimethylene trinitramine (RDX) single crystals from ∼15 to 150 cm^{-1} using the terahertz time-domain spectroscopy. We observe that all the absorption modes exhibit strong anisotropic behavior in terms of the crystal orientations. We demonstrate that the anharmonic phonon model can well describe the temperature-dependent behaviors of these absorption modes. These results indicate that the intermolecular interaction plays a major role in the collective motion of large number of RDX molecules. Our findings provide important information for understanding and controlling the dynamic properties in the explosive materials.

DOI: 10.1088/0256-307X/39/1/018701

It is believed that many kinds of materials exhibit unique spectroscopic characteristics in terahertz (THz) frequency domain.[1] The development of ultrashort lasers in last decades has led to the generation of strong coherent broadband THz wave, and hence makes it possible to probe material properties using the THz spectroscopy.[2] In particular, considering that most non-polar and non-metallic materials such as clothes, paper and plastic package only slightly absorb THz waves, THz spectroscopy is quite suitable for identifying unknown materials in the security application,[3,4] i.e., detection of the prohibited goods like drugs and explosives. In fact, explosives such as HMX, RDX, PETN, and TNT are proved to have absorption fingerprints in THz spectral range,[5–10] in contrast to their similar optical properties with the plastics or sugar in the visible and near-infrared regimes. Furthermore, absorption fingerprints are directly connected with the underlying vibration and rotation modes based on the absorption characteristics.[1] Microscopically, understanding these modes can clarify how the explosion is initiated, and thus may be pivotal to reflect the related dynamical processes under external stimuli.[11]

Among all the explosives, RDX or cyclotrimethylene trinitramine attracts a great deal of attention.[12] The large number of molecules in the RDX unit cell ($Z = 8$), compared with HMX($Z = 2$) and PETN($Z = 2$), brought unique difficulties in analysis of the vibration or rotation modes.[13,14] The absorption features in RDX have been investigated intensively in both experiments and theories.[5–10,12–19] Most of the works focused on the powder or pellets samples,[6–10,12,18] whose mixed crystal orientations result in overlapping of different absorption peaks in the spectrum, and make them difficult to distinguish experimentally. This problem becomes worse when considering that these sample properties vary significantly using different preparation techniques.[20] However, in order to unravel the intrinsic modes contributing to the absorption, reliable and unambiguous experimental data are necessarily required in order to set bases for further quantitative analysis and theoretical simulation.[9,13–15,21] One possible solution is to employ broadband THz time-domain spectroscopy (THz-TDS) to characterize the single crystals with definite orientations.[12]

Very limited works have reported the orientation-dependent THz absorption of RDX single crystals. Barber *et al.*[5] studied the absorption spectra of single crystal RDX for (210), (111) and (100) orientation using THz-TDS up to 80 cm^{-1}, and different absorption for specific orientation are observed. A continuation of the above-mentioned work[19] reported the measurements on RDX for (100), (010) and (001) directions. Based on these investigations, several issues are still unclear or unexplored in RDX single crystals: (1) no clear absorption modes observed above 100 cm^{-1} due to the limitation of THz bandwidth in the previous experiments, and (2) no quantitative discussions of temperature-dependent experimental data, which fail to directly compare the theoretical calculations with

*Corresponding author. Email: chychen@fudan.edu.cn
© 2022 Chinese Physical Society and IOP Publishing Ltd

experimental results.

In this Letter, we study the absorption modes as functions of temperature in RDX single crystals for (210) and (111) orientations using the broadband THz-TDS with a cutoff frequency up to $\sim 170\,\mathrm{cm}^{-1}$. Enormous absorption features are detected up to $\sim 120\,\mathrm{cm}^{-1}$. Using the anharmonic phonon decay model, we are able to reveal quantitatively different phonon modes across a wide temperature range.

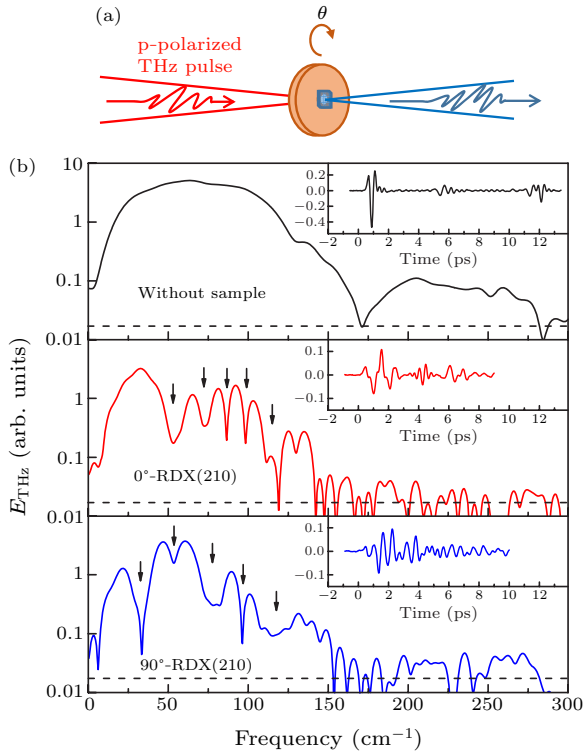

Fig. 1. (a) Schematic diagram of the sample rotation and the in-plane crystal orientation θ. (b) Frequency-domain THz signals without sample (black) and with RDX(210) of $\theta = 0°$ (red) and 90° (blue) at 100 K. The main absorption features are marked with arrows. They consistently exist at all investigated temperatures (see the following figures for details). Insets show the original time-domain signals. The dashed lines are noise floors.

High quality RDX single crystals were purchased from College of Chemical Engineering and Environment, North University of China.[22] The size of each sample is at least 4 mm × 4 mm in dimensions. The thicknesses of two (210) and one (111) samples are 0.76, 0.71 and 0.86 mm, respectively. The orientation of the crystallographic axis is verified by transmission Laue x-ray diffraction.

All measurements were performed using the broadband THz-TDS. The broadband THz wave was generated from a photoexcited spintronic THz emitter[23,24] pumped by linearly polarized femtosecond (fs) laser pulses from a Ti:sapphire laser oscillator with a pulse width of ∼35 fs, a repetition rate of 80 MHz, and a central wavelength of 800 nm. The as-generated THz beam was focused on the sample, and the transmitted THz beam was detected by the electro-optic sampling technique through a 0.5-mm-thick ZnTe(110) crystal. The sample was settled in a low-temperature cryostat with a stability of ∼0.10 K, varying between 77 K and 290 K. Orientation-dependent THz measurements were conducted by continuously rotating the sample using a high-accuracy rotation motor, as illustrated in Fig. 1(a). THz spectroscopy platform was kept in the environment with a relative humidity less than 5%.[25] More setup details can be found in the Supplemental Material.

Figure 1(b) shows the results of frequency-domain signals after fast Fourier transform (FFT) processing. The black curve shows the experimental spectrum coverage of our system, which spans from $\sim 15\,\mathrm{cm}^{-1}$ to $270\,\mathrm{cm}^{-1}$ without sample. A dip near $170\,\mathrm{cm}^{-1}$ is clearly observed, due to the strong phonon absorption of detecting ZnTe crystal. Two THz spectra for the (210)-oriented RDX single crystal obtained at $\theta = 0°$ and 90° are also presented in Fig. 1. Here, θ is defined as the angle between the RDX in-plane crystallographic orientation and the incident THz polarization direction, which also lies in the surface plane of the samples. Strong absorption features in the high frequency regime can be clearly observed. Note that the experimental results over $100\,\mathrm{cm}^{-1}$ have never been reported before.

The frequency-domain data can be further used to extract the absorption coefficient α or the extinction coefficient k, and the refractive index n via the Kramers–Kronig relation (see the Supplemental Material). The absorption coefficient α can be calculated using the equation[26–28]

$$\alpha(f) = -\frac{2}{t}\ln\left|\frac{E_{\text{with sample}}(f)}{E_{\text{without sample}}(f)}\right| + \frac{1}{t}\ln(1-R), \quad (1)$$

where t is the thickness of sample, f is frequency, E is the THz signal of electric field strength, and R is the reflectivity; $\alpha(f)$ is mainly determined by the first term on the right-hand side due to the small R values.[6,18]

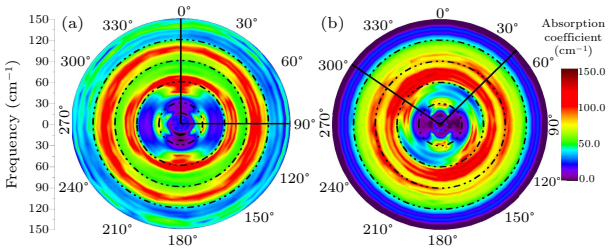

Fig. 2. Orientation-dependent absorption coefficient spectra of (a) RDX(210), (b) RDX(111) up to $150\,\mathrm{cm}^{-1}$ at 290 K. The radius represents the wavenumber of spectrum and the angle is the in-plane orientation θ. Dot-dashed circles denote $30\,\mathrm{cm}^{-1}$ increments. The bold lines mark the orientations for the following temperature dependent analysis. The contours are measured of a full 360°-rotation per 10°.

Figure 2 shows the θ-dependent absorption coefficient α of RDX(210) and RDX(111) using Eq. (1). Data were obtained as the RDX sample rotated by 360° per 10° at room temperature. The α radial contours cover the region from 15 cm^{-1} to 150 cm^{-1} and exhibit abundant absorption features, which are highly dependent on θ.

For (210)-oriented RDX single crystal, the THz absorption spectrum shows mirror symmetry along certain crystal orientations. Along axis with $\theta = 0°$, broadband absorption from 48 cm^{-1} to 68 cm^{-1} and from 103 cm^{-1} to 111 cm^{-1} are observed. By contrast, along the axis with $\theta = 90°$, broadband absorptions from 26 cm^{-1} to 35 cm^{-1}, from 66 cm^{-1} to 77 cm^{-1}, and from 100 cm^{-1} to 113 cm^{-1} are observed. The absorption around 60 cm^{-1} and 100–110 cm^{-1} persist at all θ. Based on the previous work on RDX(100),[19] $\theta = 0°$ and 90° can be most likely assigned to $\langle \bar{1}20 \rangle$ and $\langle 001 \rangle$ axes, respectively.

On the other hand, for (111)-oriented RDX, only the THz absorption spectrum below 40 cm^{-1} exhibits mirror symmetry. In particular, THz absorption is observed from 20 to 40 cm^{-1} at 0°, while the absorption is broader at 90°. In higher-frequency regime, no rotation or mirror symmetry is observed. Specifically, absorption peak is obtained at ∼45 cm^{-1}, for orientation angle between 0° and 60°. Intense THz absorption is observed around 125°, whose characteristic absorption frequency residing between 45 cm^{-1} to 53 cm^{-1} increases as θ becomes larger. At the same time, absorption between 65 cm^{-1} and 80 cm^{-1} has no well-defined relationship with the orientation angle θ. Above 90 cm^{-1}, the spectral features are intricate, consistent with previous report.[19] Only at 90°, broadband absorption from 90 to 115 cm^{-1} is obtained.

Complex structure of RDX molecules brings about innumerous vibration and rotation modes. Considering the large number of molecules in a unit cell of RDX ($Z = 8$[29]), the interactions among molecules may severely increase the complexity. Although our single crystal can reduce the problem of mixed absorption features, there are still lots of indistinguishable modes in the spectra. In principle, the vibration and rotation modes characterized by the absorption frequencies are independent of experimental setup. Note here that in Fig. 2(b), some absorption frequencies seem to vary with the θ changing, and this may be attributed to the superposition effect of many modes with the strong anisotropic absorption intensities.

Due to various modes entangled in the frequency domain, their properties are hard to identify at a given temperature. For further clarification and comparison with the theoretical data, temperature-dependent THz-TDS measurements were conducted. For RDX(210), $\theta = 0°$ and 90° are chosen since there exists mirror symmetry as shown in Fig. 2. For RDX(111), $\theta = -55°$ and 45° in Fig. 2 were chosen, since most absorption features emerge in these two directions.

Figure 3 shows the temperature-dependent absorption spectra from 80 K to 280 K. The dashed and dotted lines are fitting results described later. It can be seen that many absorption features can be well discriminated in the temperature domain. Sharp absorption peaks are denoted by yellow dotted lines, and the boundaries of broadband absorption by the red dashed lines. It is worth noting that, in Fig. 3(b), the dashed line around 38 cm^{-1} under 150 K is obtained by extrapolating the high temperature data. In fact, below ∼150 K broad absorption exists near this frequency, as also reported by previous works.[2,12]

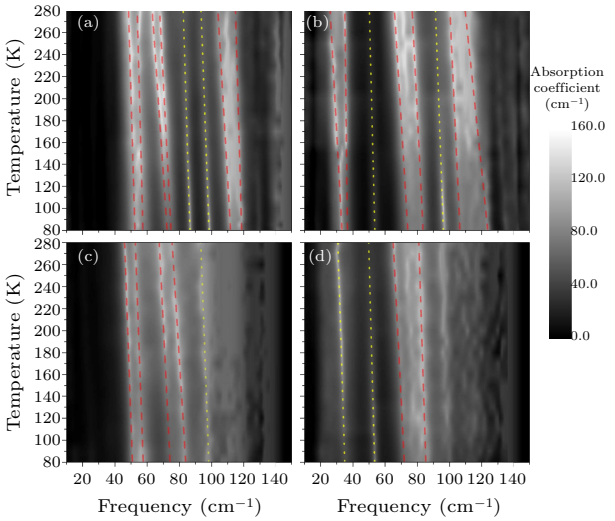

Fig. 3. Temperature-dependent absorption coefficient of (a) 0°-RDX(210), (b) 90°-RDX(210), (c) −55°-RDX(111), (d) 45°-RDX(111). The angles related to in-plane orientations based on the coordinate in Fig. 2. The temperature changed between 80 K and 280 K, and stepped by 10 K with a stability of 0.02 K. All the samples are kept in vacuum. The fitted results of peaks and boundaries by Eq. (2) are shown as yellow dotted and red dashed lines, respectively.

In Figs. 3(c) and 3(d), the data of RDX(111) above 100 cm^{-1} are quite messy and seem similar to the report on (100), (010), and (001)-oriented RDX.[19] Although previous temperature-dependent data[5] (only below 80 cm^{-1}) were obtained without knowledge of exact in-plane crystal orientation, they are coincidentally consistent with our results on 90°-RDX(210) and −55°-RDX(111). Therefore, our results provide a complete orientation-dependent measurements in a much broader spectra range.

Based on Fig. 3, a general tendency of all the absorption frequencies is their red shift with increasing temperature, although the shift magnitude for each characteristic frequency may be different. In the con-

text of solid state physics, this phenomenon is often referred to the phonon softening, which is a collective lattice behavior arising from the thermal effect. Red shift of the frequency, or the phonon softening, can be be described in general by the anharmonic phonon effect. This effect usually includes contributions from thermal expansion and anharmonic phonon-phonon coupling. Here, we employ this approximation and model those absorption frequencies $\omega = 2\pi f$ and their corresponding lifetime or widths Γ using the following equations:[30–32]

$$\begin{aligned} \omega(T) &= \omega_0 + A^{(1)}[1 + 2n(\omega_0/2)], \\ \Gamma(T) &= \Gamma_0 + A^{(2)}[1 + 2n(\omega_0/2)], \end{aligned} \tag{2}$$

where $n(\omega) = (e^{\hbar\omega/k_{\mathrm{B}}T} - 1)^{-1}$ is the Bose–Einstein distribution, ω_0 is the intrinsic harmonic frequency, and Γ_0 is the contribution due to background scattering or impurity and defect scatterings. $A^{(1)}$ and $A^{(2)}$ are fitting parameters.

The typical fitted results of an absorption peak in (210)-oriented RDX single crystal are shown in Fig. 4. Here, f and Γ were extracted from clear absorption peaks via the Lorentz peak fitting. For the broadband absorption, we only focus on the frequencies of boundaries, which were determined by the first derivative of $\alpha(f)$. The extracted results at 280 K are listed in Table 1.

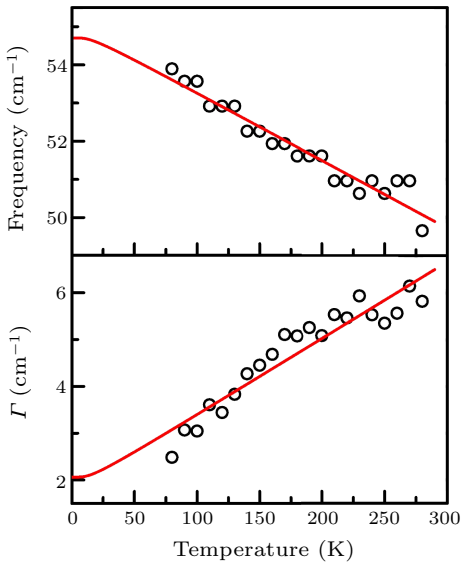

Fig. 4. The typical fitting results of the oscillation frequency f and the damping rate Γ in 90°-RDX(210). The circles are extracted data and the red curves are fits using the anharmonic effect model.

Table 1. Absorption extracted and fitted in (210)- and (111)-oriented RDX. It is worth noting that, in the mode assignments (OR, optical rotation; OT, optical translation), the correction in parentheses are contributed by solid-state modes considering intermolecular effects. For further details please refer to Ref. [14].

f_0(0 K) (cm^{-1})	f(280 K) (cm^{-1})	Orientation	Calculation[13]	Calculation[14]	Mode assignment[14]
34.3–37.4	26.8–34.6	90°-(210)		32.7	OR in C + 59.3
36.8	31.4	45°-(111)	35	36.3	OR in AB,BA
					+ NO_2 wagging and ring twisting
55.1	49.6	45°-(111)	49	52	59.3 (−7.3)
55.2	50.34	90°-(210)		57.8	NO_2 wagging
54.2–59.1	48.3–54.9	0°-(210)	59	59.3	NO_2 wagging and ring bending
53.0–59.7	45.7–52.9	−55°-(111)		60.3	59.3 (+1.0)
76.3–77.8	63.4–67.9	0°-(210)	74	74.2	OR in C
74.8–87.2	65.0–81.0	45°-(111)		83.2	NO_2 Twisting
				84.3	NO_2 wagging(+26.5)
77.6–86.5	66.6–76.7	90°-(210)		84.7	OT in B
77.1–87.5	67.9–74.2	−55°-(111)		87.0	NO_2 wagging and ring twisting (+40.3)
88.4	83.4	0°-(210)	92	88.8	OR in C + 57.8
98.3	91.9	90°-(210)		98.4	NO_2 twisting
100.6	93.2	−55°-(111)			
100.7	94.3	0°-(210)		101.7	57.8 (+43.9)
109.2–129.6	100.3–113.0	90°-(210)		108.5	NO_2 twisting
				112.7	98.4 (+43.9)
				114.4	57.8 + 108.5
115.1–120.6	103.9–114.9	0°-(210)		119.9	83.2 (+36.7)
				125.3	83.2 (+42.1)

It can be seen from Fig. 3 that our fitted results, indicated by the yellow dotted and red dashed lines, are in excellent agreement with the experimental data. This finding strongly confirms the suitability and reliability of the anharmonic phonon model applied on the RDX system. As we know, the anharmonic model is used to describe the collective behavior of the lattices that includes the fundamental coupling between the neighboring lattice sites. Clearly, successful application of this model implies that there exists some type of effect interaction between the molecules in RDX.

The fitted values of $f_0 = \omega_0/2\pi$ at 0 K using the anharmonic model are listed in Table 1, while two cal-

culations with and without interactions[13,14] are also included for comparison. The assignments of modes are also included to clarify the origin of each mode. Our result of f_0 shows a great self-consistency, as many absorption peaks and boundaries from different orientations coincide with each other. Especially, for frequency below $\sim$88 cm^{-1}, all absorption features seem to be found in more than one orientation. We note that many features in Fig. 3 evolve into quite broad absorption band, no matter how high the signal-to-noise ratio is in the experiment. For instance, when the absorption frequency reaches 80–100 cm^{-1}, the related bandwidth can pass over 10 cm^{-1}. This phenomenon is mainly due to the coupling between normal modes and strong intermolecular interactions in this frequency range, where, as a result, the characteristic absorption frequencies, very close to each other, are inevitably mix together.[33] Previous calculations of Ref. [14] agree reasonably with our data, and again suggest that it is imperative to include the contribution of interactions between the molecules. Parameter $A^{(1)}$, which phenomenologically reflects the interaction property via the anharmonic coupling, are listed in the Supplemental Material.

In summary, the THz absorption spectra of RDX(210) and RDX(111) are presented as a function of in-plane orientation. Temperature-dependent investigations demonstrate the the collective dynamics of RDX molecules, similar to the phonons, which enables us to use the anharmonic phonon model to accurately fit the temperature-dependent frequencies and widths associated with the absorption peaks. Extracted intrinsic absorption frequencies are in good agreement with previous calculations. Therefore, our findings provide critical information about the importance of the intermolecular interactions, which should be incorporated into further understanding and controlling the dynamic properties in RDX and other related explosive materials.

We thank Professor Jingbo Qi for the helpful discussion and comments.

References

[1] Ferguson B and Zhang X C 2002 *Nat. Mater.* **1** 1
[2] Beard M C, Turner G M and Schmuttenmaer C A 2002 *J. Phys. Chem. B* **106** 7146
[3] Tribe W R, Newnham D A, Taday P F and Kemp M C 2004 *Proc. SPIE* **5354** 168
[4] Federici J, Schulkin B, Huang F, Gary D, Barat R, Oliveira F and Zimdars D 2005 *Semicond. Sci. Technol.* **20** S266
[5] Barber J, Hooks D E, Funk D J, Averitt R D, Taylor A J and Babikov D 2005 *J. Phys. Chem. A* **109** 15
[6] Choi K, Hong T, Sim K I, Ha T, Park B C, Chung J H, Cho S G and Kim J H 2014 *J. Appl. Phys.* **115** 023105
[7] Zhang L L, Zhong H, Deng C, Zhang C L and Zhao Y J 2008 *Appl. Phys. Lett.* **92** 091117
[8] Huhn A K, Saenz E, de Maagt P and Bolivar P H 2013 *IEEE Trans. Thz. Sci. Technol.* **3** 5
[9] Burnett A D, Fan W H, Upadhya P C, Cunningham J E, Edwards H G M, Kendrick J, Munshi T, Hargreaves M, Linfield E H and Davies A G 2007 *Proc. SPIE* **6549** 654905
[10] Maestrojuan I, Palacios I, Etayo D, Iriarte J C, Teniente J, Ederra I and Gonzalo R 2011 *Proc. SPIE* **8188** 81880N
[11] Zhang Y Y, Chen S, Cai Y, Lu L, Fan D, Shi J C, Huang J Y and Luo S N 2020 *Engineering.* **6** 992
[12] Melinger J S, Laman N and Grischkowsky D 2008 *Appl. Phys. Lett.* **93** 011102
[13] Huang L, Shabaev A, Lambrakos S G and Massa L 2013 *Vib. Spectrosc.* **64** 62
[14] Allis D G, Zeitler J A, Taday P F and Korter T M 2008 *Chem. Phys. Lett.* **463** 84
[15] Pereverzev A, Sewell T D and Thompson D L 2013 *J. Phys. Chem.* **139** 4
[16] Chen G, Xia M Z, Lei W, Wang F Y and Gong X D 2014 *J. Phys. Chem. A* **118** 11471
[17] Ganesh D, Venkatesh M and Chaudhary A K 2018 *Appl. Opt.* **57** 8743
[18] Palka N 2012 *Acta. Phys. Pol. A* **122** 854
[19] Whitley V H, Hooks D E, Ramos K J, O'Hara J F, Azad A K, Taylor A J, Barber J and Averitt R D 2009 *Anal. Bioanal. Chem.* **395** 315
[20] Wilkinson J, Caulder S M and Portieri A 2008 *Proc. SPIE* **6949** 694904
[21] Katz G, Zybin S, Goddard W A, I I I, Zeiri Y and Kosloff R 2014 *J. Phys. Chem. Lett.* **5** 772
[22] Wang X J, Wu Y Q, Huang F L, Hu W J and Liu Y C 2019 *Propellants Explos. Pyrotech.* **44** 870
[23] Yang D W, Liang J H, Zhou C, Sun L, Zheng R, Luo S N, Wu Y Z and Qi J 2016 *Adv. Opt. Mater.* **4** 12
[24] Zhou C, Liu Y P, Wang Z, Ma S J, Jia M W, Wu R Q, Zhou L, Zhang W, Liu M K, Wu Y Z and Qi J 2018 *Phys. Rev. Lett.* **121** 086801
[25] Qi J 2021 *Sci. Sin. Phys. Mech. Astro* **51** 047404
[26] Ganesh D, Rao E N, Venkatesh M, Nagarjuna K, Vaitheeswaran G, Sahoo A K and Chaudhary A K 2020 *ACS Omega* **5** 2541
[27] Ruggiero M T 2020 *J. Infrared Millim. Terahertz Waves* **41** 491
[28] Jepsen P U and Fischer B M 2005 *Opt. Lett.* **30** 1
[29] Choi C S and Prince E 1972 *Acta Cryst. B* **28** 2857
[30] Balkanski M, Wallis R and Haro E 1983 *Phys. Rev. B* **28** 1928
[31] Menendez J and Cardona M 1984 *Phys. Rev. B* **29** 2051
[32] Tang H and Herman I P 1991 *Phys. Rev. B* **43** 2299
[33] Zhang F, Wang H W, Tominaga K and Hayashi M 2016 *WIREs Comput. Mol. Sci.* **6** 386

Supplementary Material for "Temperature-Dependent Far-Infrared Absorption in RDX Single Crystals Using Broadband Time-Domain Terahertz Spectroscopy"

1. Experimental setup

As shown in Fig. S1, the terahertz time-domain spectroscopy (THz-TDS) was employed via a degenerate pump-probe scheme using a Ti:sapphire laser oscillator that produces ~35 fs pulses at the THz emitter position, with a repetition rate of 80 MHz at a center wavelength of 800 nm (~1.55 eV) with a bandwidth of ~40 nm. Detail information about the THz emitter Fe-Pt film can be found in Refs. [1,2]. Lock-in technique was used to collect the signals with the help of an AOM (acousto-optic modulator, not shown in Fig. S1). To obtain the data with high signal-to-noise ratio, each set of data was repeated 12 times to average.

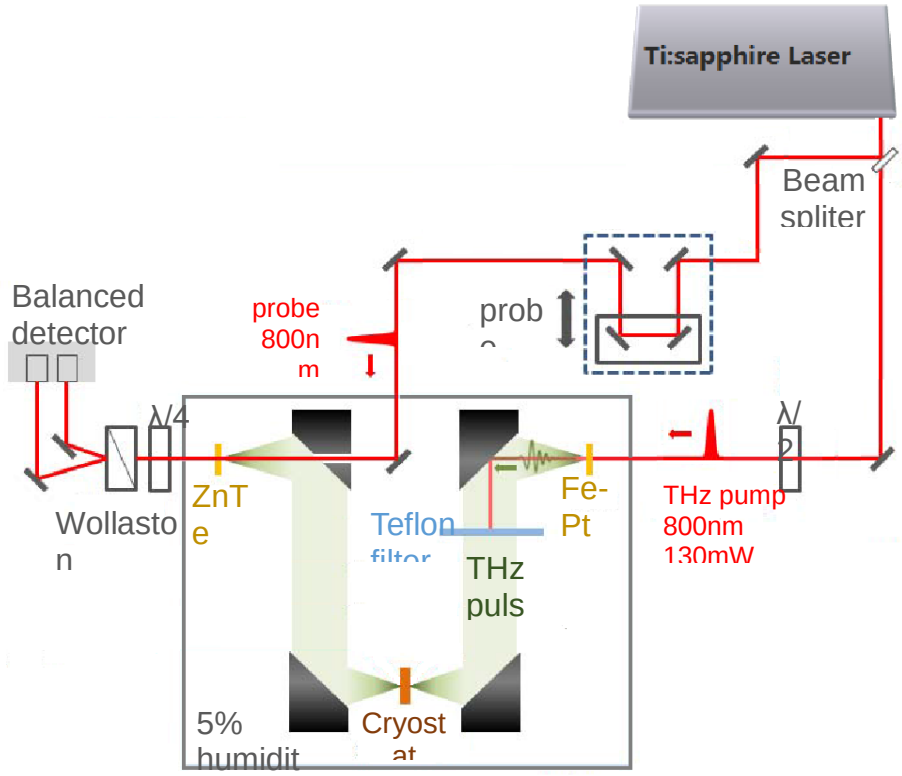

Fig. S1 Schematic diagram of the terahertz time-domain spectroscopy

2. Data processing of FFT

As shown in Figure 1(b) inset of the main text, there is a second THz pulse signal appearing at ~5 ps after the main THz pulse in the time domain even without sample. This arises from the backward and forward reflections of the pump light in the Al_2O_3 substrate of the spintronic THz emitter. Similarly, the third THz pulse signal at ~10 ps arises from the ZnTe crystal. To obtain the frequency domain information, only the data before the second THz pulse (~5.6 ps) are chosen for the fast Fourier Transform (FFT).

The time step of our original data is 20 fs and no interpolation is applied before FFT. To preserve as much signal information as possible, rectangle window is applied during FFT.

The lower frequency limit of our detection is set to ~15 cm^{-1}, due to the low frequency noise up to 7 cm^{-1}. The upper limit is set to 150 cm^{-1}, as the noise floor appears at ~170 cm^{-1}. Noise signals can be seen in the Fig. 1 of the main text.

3. Extracted refractive indices

We employ K-K relation, because it is almost impossible to correctly extracting the phases of the signals in our sample via the reference signals. As we know, the phase is proportional to the sample thickness and the THz frequency. During FFT, the phase is constrained between 0 and 2π. Due to our sample having large thickness compared to those nanoscale thin film, the actual phase values will exceed 2π. Therefore, the obtained values via FFT will have a zigzag-like feature in the frequency domain, where we need to add $2n\pi$ ($n=1,2\cdots$) at the jump points to shift up the related phases and get the correct values. However, the single crystals we used are too thick and can cause strong absorption around those characteristic absorption frequencies. Consequently, large noise is introduced during FFT at those frequencies, and leads to additional false jump points in the phase. Such result is clearly not what we want. Due to the RDX single crystals too fragile, it is impossible to get very thin samples. The above issue cannot be resolved. Therefore, the K-K relation was finally used in our calculations.

The refractive index is calculated using Kramers-Kronig relationship [3]:

$$k(f) = \frac{4\pi}{\lambda_0}\alpha(f)$$

(S1)

$$n(f) = 1 + \frac{2}{\pi} \int_{0, f' \neq f}^{\infty} \frac{f' k(f') - \omega k(f)}{f'^2 - f^2} df'$$

Here, k is the extinction coefficient, f is the frequency (cm^{-1}), λ_0 is the wavelength corresponding to f. Absorption coefficient $\alpha(f)$ is calculated considering only the transmittance component (first term in Eq.1 in the main text). As shown in second formula, the accuracy of refractive index $n(f)$is highly dependent on the frequency range of $\alpha(f)$. Thus, we put our measured $\alpha(f)$ together with high frequency data from Refs.[3][4] to extend the frequency range up to 3700 cm^{-1}. The refractive indices at 5 typical temperatures are shown in Fig. S2.

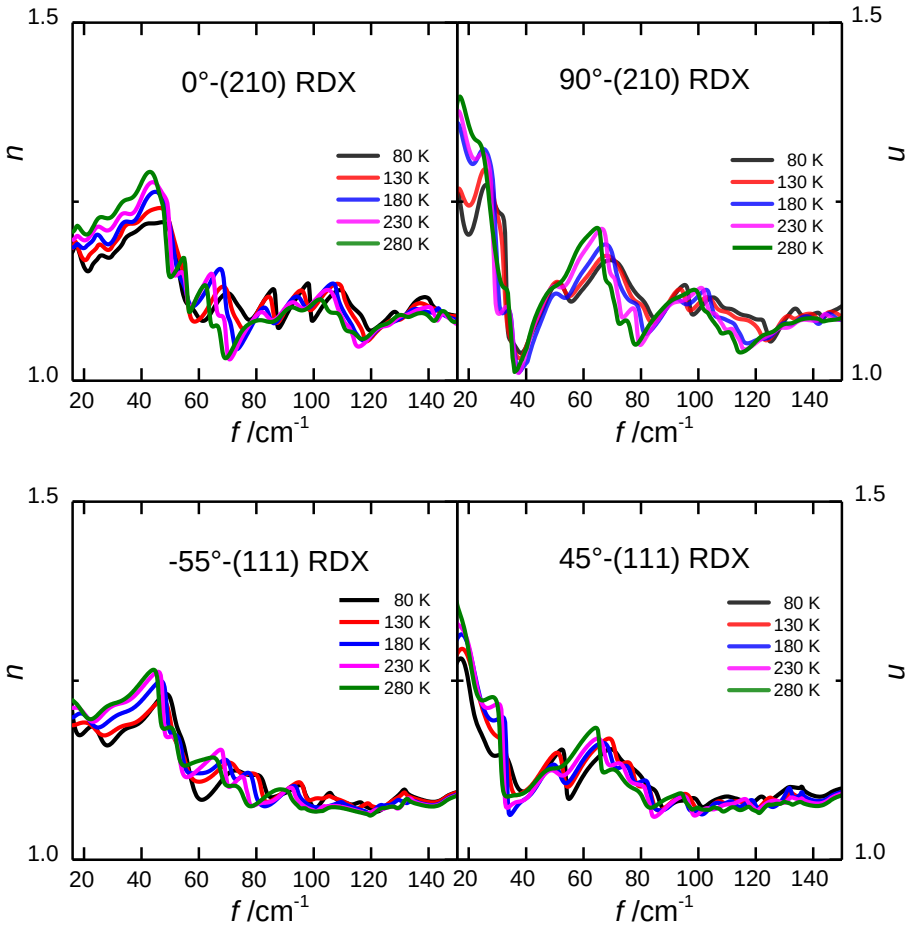

Fig. S2 Temperature-dependent refractive indices of 0°-(210)RDX, 90°-(210)RDX, -55°-(111)RDX, and 45°-(111)RDX. The in-plane orientation is corresponding to Fig. 2 in the main text.

4. Reflection correction term

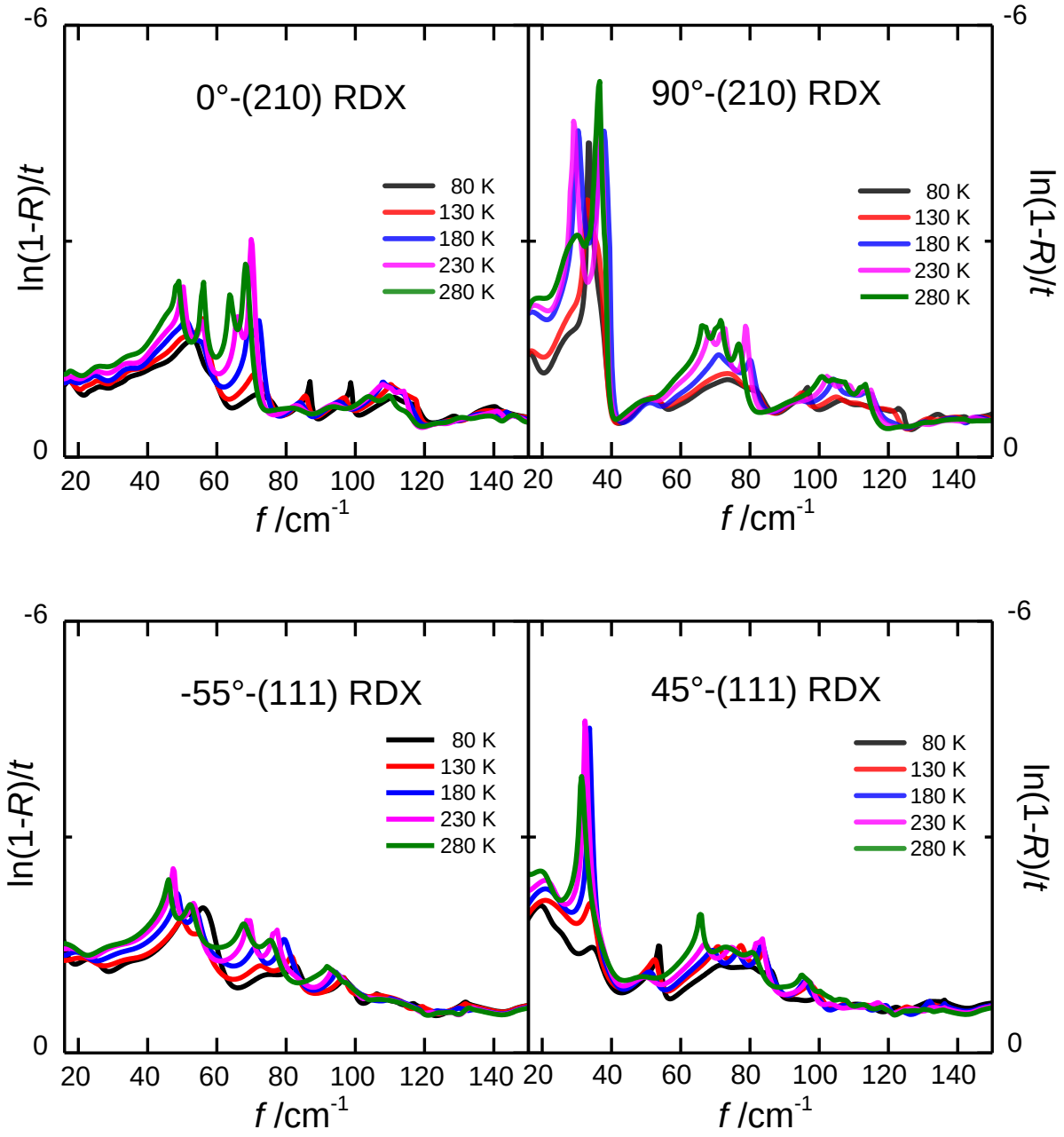

Fig. S3 Temperature-dependent reflection correction term of 0°-(210)RDX, 90°-(210)RDX, -55°-(111)RDX, and 45°-(111)RDX. The in-plane orientation is corresponding to Fig. 2 in text.

Absorption coefficient $\alpha(f)$ is extracted based on:

$$E^2_{\text{with sample}}(f) = E^2_{\text{without sample}}(f) \cdot (1-R) \cdot \exp(-\alpha t)$$

$$=> \alpha(f) = -\frac{2}{t}\ln\frac{E_{\text{with sample}}}{E_{\text{without sample}}} + \frac{1}{t}\ln(1-R) \tag{S2}$$

As mentioned in the main text, there is a reflection correction term $\frac{1}{t}\ln(1-R)$. Here, reflectivity R is given by Fresnel formula:

$$R(f) = \frac{(n-1)^2 + k^2}{(n+1)^2 + k^2} \tag{S3}$$

Results of correction term based on Eq. S1 and S3 are shown in Fig. S3. Considering the magnitude of term $-\frac{2}{t}\ln\frac{E_{\text{with sample}}}{E_{\text{without sample}}}$ (> 100 cm^{-1}), this correction term is proved relative small. The reflection correction is added to $\alpha(f)$ in Figs. 2 and 3 in our text.

5. Dynamic range of absorption

Sometimes the sample is too thick resulting in a discontinuous extrema value for the absorption coefficient. We thus establish the dynamic range as an upper limit of the detectable absorption coefficient. The specific calculation equation is [5]:

$$\alpha_{MAX}(f) = -\frac{2}{t}\ln\frac{E_{\text{noise level}}}{E_{\text{without sample}}(f)} \tag{S4}$$

Here, $\alpha_{MAX}(f)$ is the dynamic range, t is the sample thickness, $E_{\text{without sample}}(f)$ is the THz signal without a sample, and $E_{\text{noise level}}$ is the noise level independent of frequency. It worth noting that the right side of the Eq. S4 is the parameter of the experimental setup and is independent of the sample. The example of dynamic range cutoff is shown in Fig. S4. All the absorption data shown in the main text, also included in Fig. 2 and Fig. 3, take the dynamic range into account. We also redraw Fig. 3 in shape of lines in Fig. S5 at 5 typical temperatures, for the data can be easily assessed. Fitting parameters of phonon modes are listed in Table. S1.

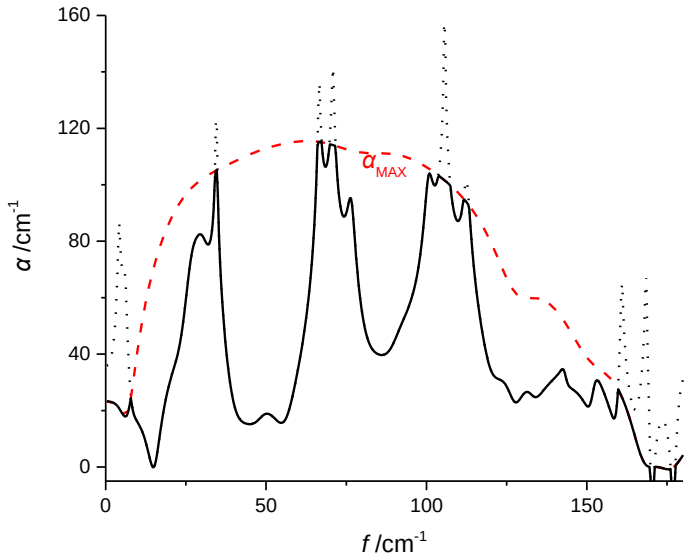

Fig. S4 Temperature-dependent absorption coefficient of (210)-90° RDX at 280 K. Red dashed line is the dynamic range. Black dotted/solid lines are the cut off/ retained parts.

Table. S1 Fitting parameters

Orientation	f_0 (0 K)/ cm^{-1}	$A^{(1)}$/ cm^{-1}
0°-(210)	54.2-59.1	0.39/0.38
	76.5-78.0	1.30/1.00
	88.5	0.67
	100.7	0.91
	115.5-120.6	1.67/0.85
90°-(210)	36.3-37.4	0.48/0.11
	55.1	0.34
	98.4	0.87
	77.7-86.6	1.17/1.07
	109.4-130.3	1.24/3.39
-55°-(111)	53.0-59.8	0.47/0.53
	77.20-87.68	0.94/1.35
	100.6	0.92
45°-(111)	36.8	0.29
	55.1	0.37
	74.9-87.3	0.93/0.70

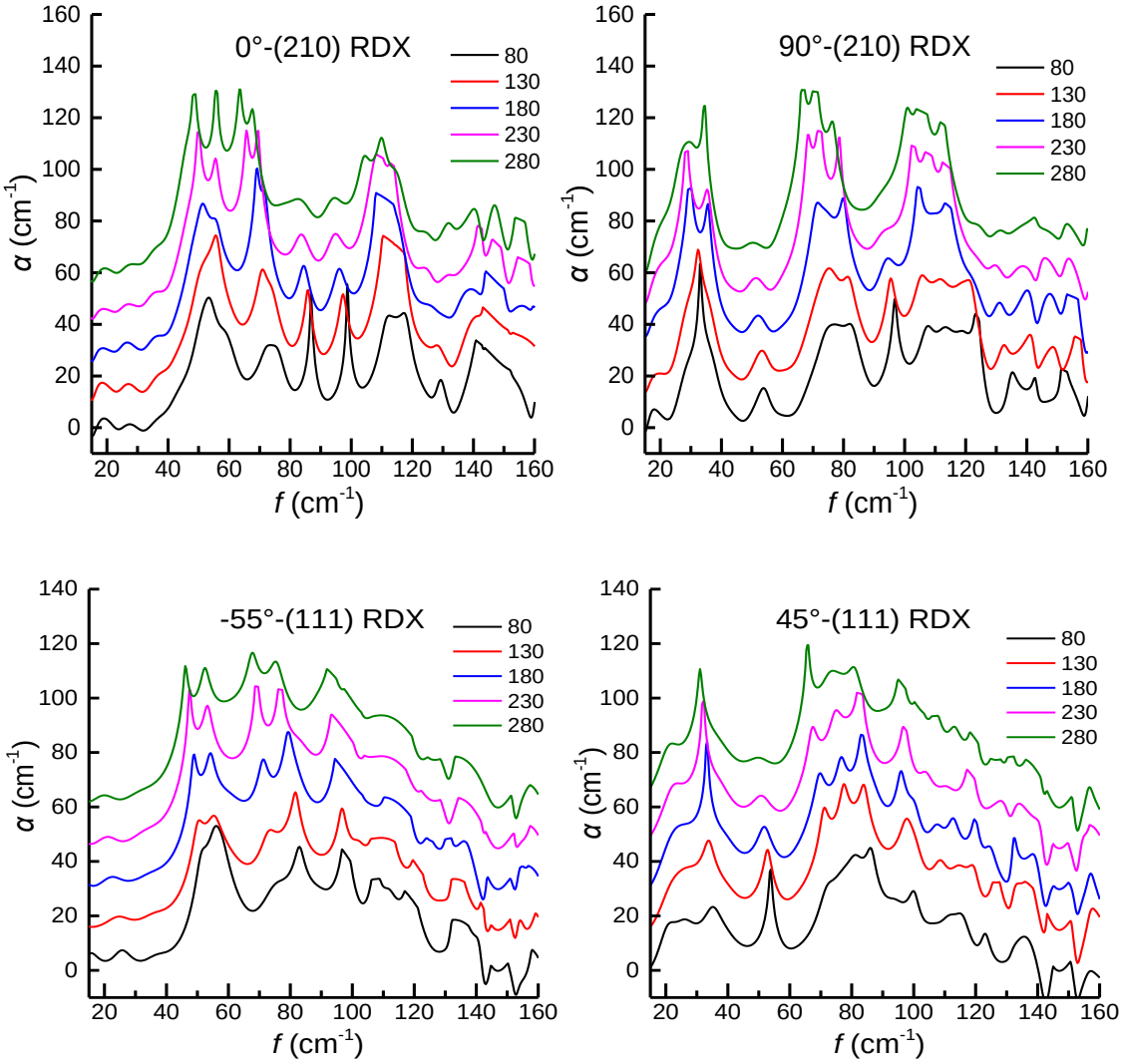

Fig. S5 Temperature-dependent absorption coefficient spectra. The stack constant of the vertical axis α is set to 15 cm^{-1} for a clearer view.

[1] D. W. Yang, J. H. Liang, C. Zhou, L. Sun, R. Zheng, S. N. Luo, Y. Z. Wu and J. Qi, Adv. Optical Mater. 4, 12 (2016).

[2] C. Zhou, Y. P. Liu, Z. Wang, S. J. Ma, M. W. Jia, R. Q. Wu, L. Zhou, W. Zhang, M. K. Liu, Y. Z. Wu, and J. Qi, Phys. Rev. Lett. 121, 086801 (2018).

[3] R. A. Isbell and M. Q. Brewster, Propellants, Explosives, Pyrotechnics 23, 218±224 (1998)

[4] S. W. Sharpe, T. J. Johnson, D.M. Sheen and D.A. Atkinson, Proc. of SPIE Vol. 6378 63780A-1

[5] P. U. Jepsen and B. M. Fischer, Opt. Lett. 30, 1 (2005).